

# Carrier lifetime measurement in $n^-$ 4H-SiC epilayers

P. B. Klein<sup>a)</sup>

Naval Research Laboratory, Washington, DC 20375, USA

(Received 3 October 2007; accepted 26 November 2007; published online 5 February 2008)

The effects of measurement technique and measurement conditions (e.g., injection level, temperature) on measured carrier lifetimes in  $n^-$  4H-SiC epilayers are investigated both experimentally and through detailed carrier dynamics simulations to better understand differences between reported lifetimes. Three common, optically based techniques are compared: time resolved photoluminescence, transient free carrier absorption, and microwave photoconductivity decay. From the details of these measurement techniques it is shown from both theory and experiment that for the limits of high or low injection, these techniques can reflect very different lifetimes. The effect of measurement conditions on the carrier lifetime was approached by simulating the carrier dynamics assuming a dominant  $Z_1/Z_2$  defect in order to calculate the evolution of the lifetimes and the carrier and defect charge state concentrations for arbitrary injection level or temperature, as a closed-form solution to this problem does not exist. The simulated behavior was found to be in reasonable agreement with experiment and the resulting values for the electron and hole capture cross sections for the  $0/+$  transition of  $Z_1/Z_2$  were found to be  $\sigma_{n2} \approx (2-4) \times 10^{-15} \text{ cm}^2$  and  $\sigma_{p2} \approx (1-2) \times 10^{-14} \text{ cm}^2$ , respectively. The simulations provide insight into the dominant processes controlling the lifetime and identify four distinct stages of decay. A simple expression for the ratio of high- to low-injection lifetimes is presented which compares well with experiment. The temperature dependence of the lifetime is found to be relatively weak below 500 K and thermally activated immediately above this temperature due to electron emission from the  $Z^0$  state. Electron emission from  $Z^-$  and hole emission become important only at higher temperatures. Simulations with both  $Z_1/Z_2$  and  $\text{EH}_6/\text{EH}_7$  defects suggest the latter does not contribute significantly to the lifetime in as-grown epilayers, due primarily to a small capture cross section for holes.

[DOI: [10.1063/1.2837105](https://doi.org/10.1063/1.2837105)]

## I. INTRODUCTION

As a result of its outstanding chemical and thermal stability, superior thermal conductivity, and high breakdown field, SiC has become an important material for the development of high-power microwave devices and high voltage switching devices capable of performing beyond the theoretical limitations of Si-based technology. However, in spite of the progress that has been made in both materials growth and device fabrication, material defects continue to limit the incorporation of these devices in many current applications. For high voltage, bipolar switching devices, an area of particular concern has been the high forward voltage drop that is developed across the thick, low-doped  $n^-$  drift region, which results in excessive heat dissipation during the switch on-cycle. Ideally, the forward voltage drop is minimized by conductivity modulation, where a high concentration of majority and minority carriers are injected into the drift region under high forward bias, thus raising the conductivity of the layer. The carrier concentration that can be injected is directly limited by the carrier lifetime, which is controlled by material defects.

During operation, such devices run under high injection, so the high-injection lifetime is of particular interest. However, the achievement of the high degree of base modulation necessary for good device performance depends upon the

effectiveness of conductivity modulation. This requires long carrier lifetimes, particularly for the minority holes, since the majority carrier traps at equilibrium are already filled. Without a long minority carrier lifetime (MCL), the achievable base modulation will therefore be limited and the forward voltage drop will be excessive. Thus, the MCL is a particularly important parameter for bipolar structures. As Levinshtein *et al.* have noted:<sup>1</sup> “Just this parameter controls the degree of base modulation by minority carriers at high injection levels, residual voltage drop across the devices at high current densities, switch-on and switch-off times, critical charge density in the thyristors, etc... ”

Consequently, there has been considerable interest in characterizing the lifetimes of carriers within epitaxial layers and within complete device structures, although the relationship between these is not always clear.<sup>1</sup> However, wide variations in measured lifetimes are not uncommon in the literature and even comparison of different measurements on the same sample can yield substantially different results. As we will show, this stems from basic differences between measurement techniques and from differences in experimental conditions, such as injection level, temperature, and surface condition. Different measurement techniques are often sensitive to very different physical parameters, thus leading to the determination of qualitatively different lifetimes. Variations in injection level and temperature can significantly affect the carrier dynamics and, consequently, the carrier life-

<sup>a)</sup>Electronic mail: [klein@bloch.nrl.navy.mil](mailto:klein@bloch.nrl.navy.mil).

Report Documentation Page				Form Approved OMB No. 0704-0188	
Public reporting burden for the collection of information is estimated to average 1 hour per response, including the time for reviewing instructions, searching existing data sources, gathering and maintaining the data needed, and completing and reviewing the collection of information. Send comments regarding this burden estimate or any other aspect of this collection of information, including suggestions for reducing this burden, to Washington Headquarters Services, Directorate for Information Operations and Reports, 1215 Jefferson Davis Highway, Suite 1204, Arlington VA 22202-4302. Respondents should be aware that notwithstanding any other provision of law, no person shall be subject to a penalty for failing to comply with a collection of information if it does not display a currently valid OMB control number.					
1. REPORT DATE <b>OCT 2007</b>		2. REPORT TYPE		3. DATES COVERED <b>00-00-2007 to 00-00-2007</b>	
4. TITLE AND SUBTITLE <b>Carrier lifetime measurement in n&amp;#8722; 4H-SiC epilayers</b>				5a. CONTRACT NUMBER	
				5b. GRANT NUMBER	
				5c. PROGRAM ELEMENT NUMBER	
6. AUTHOR(S)				5d. PROJECT NUMBER	
				5e. TASK NUMBER	
				5f. WORK UNIT NUMBER	
7. PERFORMING ORGANIZATION NAME(S) AND ADDRESS(ES) <b>Naval Research Laboratory,4555 Overlook Avenue SW,Washington,DC,20375</b>				8. PERFORMING ORGANIZATION REPORT NUMBER	
9. SPONSORING/MONITORING AGENCY NAME(S) AND ADDRESS(ES)				10. SPONSOR/MONITOR'S ACRONYM(S)	
				11. SPONSOR/MONITOR'S REPORT NUMBER(S)	
12. DISTRIBUTION/AVAILABILITY STATEMENT <b>Approved for public release; distribution unlimited</b>					
13. SUPPLEMENTARY NOTES					
14. ABSTRACT					
15. SUBJECT TERMS					
16. SECURITY CLASSIFICATION OF:			17. LIMITATION OF ABSTRACT  <b>Same as Report (SAR)</b>	18. NUMBER OF PAGES  <b>14</b>	19a. NAME OF RESPONSIBLE PERSON
a. REPORT <b>unclassified</b>	b. ABSTRACT <b>unclassified</b>	c. THIS PAGE <b>unclassified</b>			

TABLE I. Characteristics and fitted parameters for the three  $n^-$  4H-SiC epitaxial layers. All epilayers were grown on  $n^+$  substrates by silane-based MOCVD.

Sample $\rightarrow$	A	B	C
Format	3" wafer	$\approx 1 \text{ cm}^2$	$\approx 1 \text{ cm}^2$
Thickness ( $\mu\text{m}$ )	160	52	160
$n_0 = N_d - N_a$ ( $\text{cm}^{-3}$ )	$4 \times 10^{14}$	$1 \times 10^{15}$	$4 \times 10^{14}$
$N$ ( $\text{cm}^{-3}$ ) <sup>a</sup>	$2.7 \times 10^{13}$	$5.6 \times 10^{12}$	$1.1 \times 10^{13}$
$\sigma_{n2}$ ( $\text{cm}^2$ ) <sup>a</sup>	$3.5 \times 10^{-15}$	$1.8 \times 10^{-15}$	$3 \times 10^{-15}$
$\sigma_{p2}$ ( $\text{cm}^2$ ) <sup>a</sup>	$1.4 \times 10^{-14}$	$1 \times 10^{-14}$	$1.4 \times 10^{-14}$

<sup>a</sup>Parameters determined in this work by fitting experimental data to the result of the carrier dynamics simulations.

times. This was of particular interest in the original work of Shockley and Read.<sup>2</sup> The bulk recombination rate can also be masked by surface recombination, depending upon the quality of the surface and of the interface between the epitaxial layer and the substrate.

All of these issues conspire to make comparisons between measured lifetimes somewhat ambiguous. Here we examine the variations of measured lifetimes in  $n^-$  4H-SiC epitaxial layers with the specific technique chosen for the measurement and with the variations in local environment under which the measurement is carried out. The latter is addressed by experiment and by detailed carrier dynamics simulations, since the recombination kinetics at defects cannot, in the general case, be expressed by a simple analytical formulation. These calculations provide insight into the variations in the carrier lifetime for arbitrary injection level or temperature and can be compared to experimentally measured behavior. The results help to elucidate the dominant processes controlling the lifetime under varying experimental conditions and provide a basis for comparison between measured lifetimes.

## II. EXPERIMENTAL

Carrier lifetime studies of three 4H-SiC epilayers are reported here in order to compare directly to the carrier dynamics simulations and to provide examples of the behavior discussed in the text. The comparison of measured and calculated behavior also provides a method for determining two important capture cross sections, not uniquely available in the literature, that are necessary to carry out the simulations for the general case. The characteristics of three samples employed in the measurements, labeled A, B, and C, are summarized in Table I. All were grown by silane-based metalorganic chemical vapor deposition (MOCVD) on  $n^+$  4H-SiC substrates.

Time-resolved photoluminescence measurements were generally carried out at 300 K in order to ensure a well-thermalized carrier population. A flow-through optical cryostat or a temperature-regulated heat stage was used for temperature-dependent measurements. Excitation was provided by either a frequency-tripled, Q-switched Nd:yttrium-aluminum-garnet (YAG) laser (355 nm, 4 ns pulse width, 1–30 Hz, 0–2 mJ/pulse) or a frequency doubled, cavity-dumped, mode locked Ti:sapphire laser (355 nm, 130 fs pulse width, <0.1–1 MHz, 0–5 nJ/pulse). The collected

light was dispersed by a 0.22 m double spectrometer and detected by a GaAs photomultiplier and time correlated single photon counting. Transient free carrier absorption measurements employed the Nd:YAG laser as a pump source, a continuous wave, 1310 nm diode laser (0–5 mW) probe beam, and a 0.3 mm diameter InGaAs detector matched to a transimpedance amplifier. Microwave photoconductivity decay ( $\mu$ -PCD) measurements were carried out with a Semilabs WT-85 lifetime scanner that was converted to include 355 nm excitation and 10 ns temporal resolution.

Since the incident 355 nm light has a penetration depth of about 50  $\mu\text{m}$ ,<sup>3,4</sup> the carrier injection levels vary with depth. Consequently, experimental injection levels represent averages over the layer thickness. Here, the average injection level was determined by evaluating the injection at an effective depth  $z_{\text{eff}}$  corresponding to equal numbers of absorbed photons above and below that depth,  $z_{\text{eff}} = \alpha^{-1} \ln[2/(1 + e^{-\alpha d})]$ , where  $\alpha$  is the absorption coefficient at 355 nm and  $d$  is the layer thickness.

## III. COMPARING OPTICALLY BASED CARRIER LIFETIME MEASUREMENT TECHNIQUES

Previous studies comparing the results of different carrier lifetime measurement techniques have been primarily focused on Si and on electrical techniques that are directly applicable to device structures, such as surface photovoltage,<sup>5–7</sup> open circuit voltage decay (OCVD),<sup>1,8</sup> reverse recovery (RR),<sup>1,8</sup> and electrolytic metal tracer<sup>5,6</sup> measurements. (An overview of the most commonly used optical and electrical lifetime measurement techniques is given by Schroder.<sup>9</sup>) Optically based measurements, such as  $\mu$ -PCD (Refs. 5–7) and time-resolved photoluminescence (TRPL),<sup>8</sup> have also been included in a few of these reports. In general, these studies have been concerned with the specific conditions under which different measurements can give similar results or with the source of the disagreement between techniques. For example, Levinshtein *et al.*<sup>1</sup> determined that the very short lifetimes determined from RR measurements were the result of a poor  $p^+/n^-$  interface within the  $p-i-n$  structure (i.e., a thin layer of short lifetime). These lifetimes were found to be much shorter than those determined by OCVD measurements on the same structure because the RR technique is specific to the region near the junction, while the OCVD measurement samples the much larger width of the drift region.

In this work we focus on optical techniques, which are nondestructive and require no device structure, making them attractive for materials characterization. While there are many approaches to carrier lifetime measurement, we have chosen three common techniques that are also available in our laboratory: TRPL, transient free carrier absorption (TFCA), and  $\mu$ -PCD.

Measured carrier lifetimes are controlled by several competing recombination processes: The contributions of carrier capture and thermal emission at defect levels was first considered in detail by Shockley and Read<sup>2</sup> and by Hall<sup>10</sup> (SRH). Radiative emission is dominant in direct band gap materials but provides a much smaller contribution to recom-

bination in indirect gap semiconductors such as SiC. At high injection levels [ $>10^{18} \text{ cm}^{-3}$  in 4H-SiC (Refs. 11 and 12)] three-particle Auger recombination becomes dominant. In addition to these bulk recombination processes, high concentrations of defects at the surface or at an interface can also trap carriers effectively. The measured lifetime,  $\tau_{\text{meas}}$ , is determined by the sum of these contributions

$$\frac{1}{\tau_{\text{meas}}} = \frac{1}{\tau_{\text{SRH}}} + \frac{1}{\tau_{\text{Rad}}} + \frac{1}{\tau_{\text{Auger}}} + \frac{1}{\tau_{\text{Surf}}}. \quad (1)$$

For 4H-SiC, we will consequently neglect the radiative contribution and generally limit the injection levels to  $<10^{18} \text{ cm}^{-3}$ , so that Auger recombination can be neglected as well. Surface recombination can make a significant contribution to the measured lifetime and is considered in more detail later in this section. For the present, we consider bulk lifetimes dominated by SRH processes occurring at defects. While the SRH model focused on steady-state conditions, we consider here the transient case, where the nonequilibrium carrier and defect concentrations decay back to their equilibrium levels after a short, above-gap optical pulse.

Carrier lifetimes in general are injection dependent, with well-defined limits at very high and very low injection. In the low-injection limit, where the injected majority carriers are just a perturbation to the equilibrium carrier concentration, the lifetime is controlled by the minority carriers and approaches the minority carrier lifetime,  $\tau_{\text{MCL}}$ . Under high injection conditions, the nonequilibrium electron and hole concentrations,  $\delta n(t)$  and  $\delta p(t)$ , respectively, are approximately equal (to within the small concentration of trapped carriers):  $\delta n \approx \delta p$ . Consequently, the electron and hole concentrations decay at the same rate, and the instantaneous electron and hole lifetimes,  $\tau_n$  and  $\tau_p$ , respectively, are both fixed at the high-level limit  $\tau_{\text{HL}}$  until the carrier concentration has decayed sufficiently to become comparable to the equilibrium carrier concentration. With further decay, the two carrier lifetimes begin to diverge.

In the standard SRH model, the carrier lifetime increases with increasing injection between the low-level and high-level limits, as long as thermal emission from defects is relatively unimportant. For  $n^-$  4H-SiC this is generally the case at room temperature, as the dominant defects are relatively deep. Between the low and high injection limits, the SRH model predicts a carrier lifetime that increases monotonically with injection level. While the SRH model assumes a single simple defect, very low defect concentrations (such that  $\delta n = \delta p$ ) and steady-state conditions, there has been much work over the years extending the model beyond these limitations, particularly to the transient case.<sup>13–17</sup> However, there is no simple, closed-form solution that can be applied to the general case.<sup>15</sup> The absence of a simple analytical method to treat the general case has limited many studies to either the high- or low-injection limits.

Since the low- and high-injection lifetimes are also both important device parameters; it is natural to focus on these two regimes. Consequently, in considering the differences in the lifetimes determined by different experimental techniques, we will restrict these comparisons to the low- and high-level limits,  $\tau_{\text{MCL}}$  and  $\tau_{\text{HL}}$ , respectively. By considering

the details of each measurement technique, the relationship between the measured lifetimes and the decay of the electron or hole concentrations can be determined. However, in order to study the effect of arbitrary variations in injection level and temperature on the carrier lifetimes under transient conditions, we carry out in Sec. IV carrier dynamics simulations, where the bulk recombination is modeled by capture and emission at a single dominant defect and compared to experiment.

### A. Transient free carrier absorption

The TFCA technique has been applied in Si (Refs. 18–20) as well as in SiC.<sup>21–23</sup> In this approach, a below-gap, steady-state infrared probe beam of intensity  $I_0$  is focused onto the sample, and the transmitted light of intensity  $I_1$  is collected on a fast infrared detector.  $I_1$  accounts for the steady-state losses due to reflections and absorption from the  $n^+$  substrate and from the equilibrium carrier concentration in the epilayer. When a short, above-gap pump pulse from an ultraviolet (UV) laser is incident on the same region of the sample, excess carriers  $\delta n$  and  $\delta p$  are injected. The excess carriers provide additional absorption of the infrared probe beam through free carrier absorption, so that a transient dip in transmission is sensed by the detector after the arrival of the pump pulse. As the injected nonequilibrium carriers recombine, the transmission transient decays with a rate reflecting the lifetime of the carriers as the transmission returns to its steady-state level.

In terms of the transient, nonequilibrium carrier concentrations  $\delta n(t)$  and  $\delta p(t)$ , the transmitted infrared signal can be written as<sup>18</sup>

$$I_T(t) = I_1 \exp\{-[\sigma_e \delta n(t) + \sigma_h \delta p(t)]d\}, \quad (2)$$

where  $d$  is the epilayer thickness and  $\sigma_e$  and  $\sigma_h$  are the cross sections for free carrier absorption by electrons and holes, respectively, and depend on the wavelength and polarization of the infrared probe beam with respect to the  $c$ -axis.<sup>24,25</sup>

While the UV pump light often penetrates into the substrate, the transient component from the  $n^+$  substrate is very fast and does not interfere significantly with the epilayer contribution.<sup>23</sup> With initial injection levels  $\delta n(0) = \delta p(0) \equiv g$ , the transmitted probe light intensity reaching the detector immediately after the excitation pulse ( $t=0$ ) is reduced from its initial steady-state value  $I_1$  to  $I_T = I_1 \exp[-(\sigma_e + \sigma_h)gd]$ . The magnitude of the time-varying transmission transient is  $\Delta I(t) = I_1 - I_T(t)$ ,

$$\Delta I(t) = I_1 \{1 - \exp[-(\sigma_e \delta n + \sigma_h \delta p)d]\}. \quad (3)$$

In almost all cases the epilayer absorption is relatively small, e.g.,  $\sigma_{e,h} \delta n d \ll 1$ . Therefore, the magnitude of the transmission transient representing the return of the carrier system to equilibrium follows:

$$\Delta I(t) = I_1 [\sigma_e \delta n(t) + \sigma_h \delta p(t)]d. \quad (4)$$

Under high injection conditions,  $\delta n \approx \delta p$  and  $\Delta I(t) \equiv I_1 [\sigma_e + \sigma_h] \delta n(t)d$ . Thus, the magnitude of the transmission transient, or TFCA signal, follows the high injection carrier concentration,  $\delta n(t)$ . Consequently,  $\tau_n = \tau_p = \tau_{\text{HL}}$  and the carriers



decay with the high injection lifetime. Thus, this measurement accurately reflects the high injection lifetime.

Under low injection conditions, however, we cannot assume that  $\delta n \approx \delta p$ . In general, neither the electron nor hole contribution to Eq. (4) dominates, their relative contributions are dependent upon probe wavelength and polarization.<sup>24</sup> Consequently, the TFCA lifetime at low injection is a linear combination of electron and hole components and is not simply related to  $\tau_{\text{MCL}}$ .

## B. Photoluminescence decay

At room temperature the carrier system is well-thermalized and radiative transitions across the band gap reflect the lifetime of the free carriers. In indirect gap materials such as SiC, the purely radiative lifetime of the band-band emission is quite long. Consequently, faster competing processes (e.g., carrier capture by defects), which determine the carrier lifetime, dominate the observed luminescence decay. The band-band PL intensity is of the form  $I_{\text{PL}}(t) = \gamma n(t)p(t)$ . Writing  $n(t) = n_0 + \delta n$  and  $p(t) = p_0 + \delta p$ , where  $n_0$  and  $p_0$  are the equilibrium electron and hole concentrations, and for  $n$ -type material  $p_0 \ll n_0$ ,  $\delta n$ ,  $\delta p$ , the PL intensity takes the form

$$I_{\text{PL}}(t) = \gamma [n_0 + \delta n(t)] \delta p(t). \quad (5)$$

Under low excitation conditions ( $\delta n \ll n_0$ ),  $I(t) \approx \gamma n_0 \delta p(t)$ , so the PL intensity follows the minority hole concentration. Thus, in the low injection limit the PL lifetime reflects the MCL,  $\tau_{\text{PL}} = \tau_{\text{MCL}}$ . Under high excitation conditions, however,  $\delta n \approx \delta p \gg n_0$ , so  $I_{\text{PL}}(t) \approx \gamma [\delta n(t)]^2$ . Consequently, the PL intensity decays twice as fast as the carrier lifetime, due to the bimolecular recombination kinetics. The PL decay time at high injection is then expected to be half of the high injection lifetime,  $\tau_{\text{PL}} = \frac{1}{2} \tau_{\text{HL}}$ .

## C. Microwave photoconductivity decay

In the  $\mu$ -PCD technique,<sup>26</sup> one measures the fractional change in the microwave power,  $\delta P_{\mu W} / P_{\mu W}$ , reflected from the sample due to an above-gap optical pulse that provides the injected carriers. The change in reflectivity results from a change in the sample conductivity,  $\delta \sigma(t)$ , induced by the nonequilibrium carriers. For small variations in the conductivity,<sup>26</sup>  $\delta P_{\mu W} / P_{\mu W} \propto \delta \sigma(t)$ . The conductivity transient can be written as

$$\delta \sigma(t) = e [\mu_n \delta n(t) + \mu_p \delta p(t)], \quad (6)$$

where  $\mu_n$  and  $\mu_p$  are the electron and hole mobilities, respectively, and  $e$  is the electronic charge. Consequently, the measured signal takes the form

$$\frac{\delta P_{\mu W}}{P_{\mu W}} \propto [\mu_n \delta n(t) + \mu_p \delta p(t)]. \quad (7)$$

Under high injection conditions,  $\delta n \approx \delta p$  and the  $\mu$ -PCD signal decays as  $[\mu_n + \mu_p] \delta n(t)$ . As with the TFCA technique, the measured change in reflected microwave power is proportional to the high-injection carrier concentration,  $\delta n(t) = \delta p(t)$ , and the PCD decay follows the high injection carrier lifetime,  $\tau_{\text{HL}}$ .

TABLE II. The carrier lifetime measured under low- and high-injection conditions for the three optical measurement techniques. Where a single carrier lifetime is not dominant, the variation of the measured parameter with electron and hole concentration is indicated.

Injection	TFCA	TRPL	$\mu$ -PCD
High	$\tau_{\text{HL}}$	$\tau_{\text{HL}}/2$	$\tau_{\text{HL}}$
Low	$\sigma_e \delta n(t) + \sigma_h \delta p(t)$	$\tau_{\text{MCL}}$	$\mu_n \delta n(t) + \mu_p \delta p(t)$

Under low-injection conditions,  $\delta P_{\mu W} / P_{\mu W}$  varies as  $[\mu_n \delta n(t) + \mu_p \delta p(t)]$ , and the low-injection lifetime is a linear combination of electron and hole contributions, similar to TFCA. In general,  $\mu_p < \mu_n$  (in 4H-SiC,  $\mu_n \approx 900 \text{ cm}^2/\text{V s}$ ,  $\mu_p \approx 100 \text{ cm}^2/\text{V s}$ ), so the relative contribution of the electrons is enhanced at low injection. This leads to a situation in which the low-injection measurement might actually reflect the lifetime of the majority carrier rather than that of the minority carrier. In any case, it is clear that the low-injection  $\mu$ -PCD lifetime is not simply related to  $\tau_{\text{MCL}}$ .

## D. Discussion

The conclusions from the previous discussion are summarized in Table II, where for each measurement technique and for the limit of high or low injection, either the carrier lifetime that is reflected by the measurement is presented or, in cases where the measurement does not follow the decay of a single carrier, Table II gives the dependence of the measured parameter on the carrier concentrations. It is apparent that of the three optical techniques considered, the high-injection lifetime may be obtained directly from all three, assuming that the measurement is truly carried out in the high-injection limit and that the factor of 2 correction is applied to the photoluminescence (PL) decay time. This is not the case at low injection, however. While the MCL can be determined directly by low-injection PL, the corresponding measurements for the other two techniques lead, in general, to linear combinations of electron and hole contributions which are not simply related to  $\tau_{\text{MCL}}$ . For these techniques, measurement under low-injection conditions does not provide the lifetime of the minority carrier.

The caveat of carrying out the measurement in the true high-injection limit is not trivial. For example, the measured dependence of the PL lifetime upon the injection level is shown in Fig. 1(a) for a 3-in., 4H-SiC wafer with a 160  $\mu\text{m}$  thick  $n^-$  epilayer, with carrier concentration in the mid- $10^{14} \text{ cm}^{-3}$  range. The range of injections between the high- and low-injection limits exceeds two orders of magnitude, so that a measurement can be carried out well above or well below the doping level and still not have reached the high- or low-injection regimes. TFCA measurements in this material, taken at the same position on the wafer as the PL decays, are also shown for relatively high injections. The expected factor of 2 difference between the high-injection lifetimes for these two techniques (Table II) is readily apparent in the figure.

The injection dependence of the measured lifetime shown in Fig. 1(a) was found to be typical of  $n^-$  epilayers. For example, a similar measurement on an unrelated 52  $\mu\text{m}$

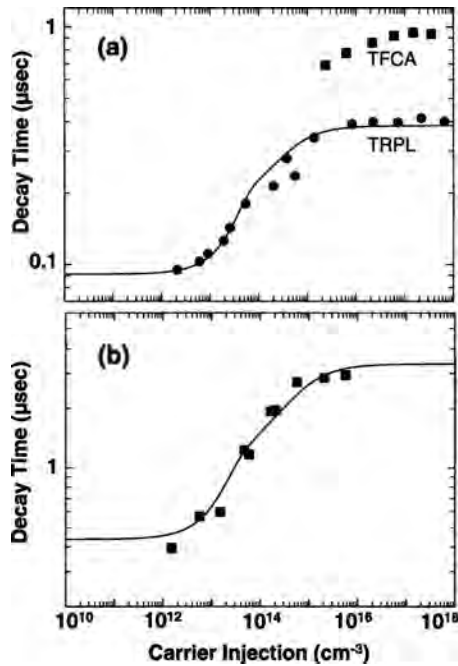


FIG. 1. Injection dependence of the PL decay time for (a) sample A and (b) sample B. The PL decay time is compared in (a) to that determined by TFCA at the same location on the sample. The factor of 2 difference in lifetime expected between these techniques is apparent. The solid lines are the result of carrier dynamics simulations described in Sec. IV.

thick epilayer (sample B) is shown in Fig. 1(b) for injection levels up to  $10^{16} \text{ cm}^{-3}$ . The injection dependence is similar to that of the thicker layer and the carrier lifetimes in this case are generally longer, presumably due to a smaller defect concentration, as the thinner layer should be more seriously affected by surface recombination, yet still exhibits considerably longer lifetimes.

A qualitative comparison between the three optical techniques can be seen in Fig. 2 in the form of lifetime maps of the 3-in. wafer of Fig. 1(a), taken with TRPL ( $1 \times 10^{16} \text{ cm}^{-3}$  injection, average lifetime  $\approx 270 \text{ ns}$ ), TFCA ( $5 \times 10^{16} \text{ cm}^{-3}$  injection, average lifetime  $\approx 600 \text{ ns}$ ), and  $\mu$ -PCD ( $> 1 \times 10^{16} \text{ cm}^{-3}$  injection, average lifetime  $\approx 700 \text{ ns}$ ). In addition to similarities in the observed spatial variation of the lifetimes, the range of the average high-injection lifetimes over the wafer tends to follow Table II reasonably well. While some of these results were obtained at injection levels slightly below the high-injection limit, it is apparent from Fig. 1(a) that they are close enough to reflect the expected similarity between the TFCA and  $\mu$ -PCD results and their differences with respect to the TRPL lifetimes.

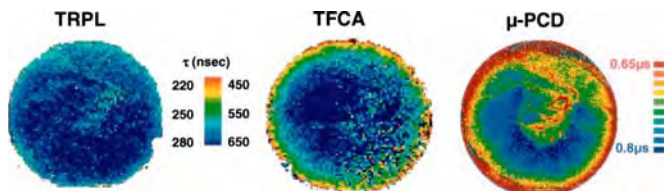


FIG. 2. (Color online) Carrier lifetime maps of sample A (3 in. wafer) determined by TRPL, TFCA, and  $\mu$ -PCD at relatively high injection ( $\approx 1 - 5 \times 10^{16} \text{ cm}^{-3}$ ). The average lifetimes reflect the conclusions in Table II for high injection.

The overall message suggested by Table II and the earlier considerations is that the validity of carrier lifetime comparisons between experimental techniques depends very much on the measurement conditions and the measurement technique employed. It is clear that care must be taken to ensure that the same physical lifetime is being probed and that environmental factors, such as injection level and temperature (considered in Sec. IV), be taken into account. These steps still leave open the possibility that the measured lifetimes of different samples will reflect different levels of surface recombination. Ideally the surface recombination velocity (SRV) could be measured independently, although this is not always practical.

### E. Surface recombination

Up until this point, the effects of surface recombination have been neglected. It is clear from Eq. (1) that there is direct competition between the bulk and surface contributions to the measured lifetime, while the discussion leading up to Table II considered only bulk lifetimes. A fast surface recombination can dominate the measured lifetime, distorting much of the injection-dependent variations suggested in Table II. The effect of the surface on the measured recombination time is generally treated by solving the carrier continuity equation with appropriate boundary conditions at the top and bottom surfaces of the layer.<sup>27</sup> The solution results in a transcendental equation for the surface contribution to the lifetime, involving the carrier diffusion coefficient  $D$ , the layer thickness  $d$ , and the SRV at each of the surfaces. Of the various approximations that are often employed to obtain a simple relationship for the surface recombination rate, a useful approach<sup>28</sup> involving a combination of the low- and high-SRV limits has been shown to exhibit very good agreement with the exact solution<sup>29</sup> and is given by

$$\frac{1}{\tau_s} = \left( \frac{d^2}{\pi^2 D} + \frac{d}{2S} \right)^{-1}. \quad (8)$$

This approximation assumes that the surface recombination velocity  $S$  is identical for both surfaces. For an  $n^-$  epilayer grown on an  $n^+$  substrate, the surface and interface recombination velocities may be quite different. In that case, the value of  $S$  determined using Eq. (8) must be regarded as an average for the layer.

The magnitude of  $S$  can vary over a wide range, depending on the nature of the surface. Depth-resolved TFCA measurements have been used to assess the SRV in a  $40 \mu\text{m}$  4H-SiC epilayer that was exposed to various surface treatments.<sup>21</sup>  $S$  was found to vary from  $5 \times 10^3 \text{ cm/s}$  for the as-grown surface to  $5 \times 10^5 \text{ cm/s}$  for a mechanically polished surface. Similarly, TRPL studies determined a SRV of  $2.5 \times 10^3 \text{ cm/s}$  for the as-grown surfaces of a set of 4H-SiC samples with varying layer thicknesses.<sup>30</sup> Thus, taking  $S \approx 5000 \text{ cm/s}$  for the as-grown  $160 \mu\text{m}$  thick layer of Fig. 1, Eq. (8) can be employed to estimate the high-injection surface recombination rate, with the ambipolar diffusion coefficient<sup>31</sup>  $D_a \approx 3 \text{ cm}^2/\text{s}$ . For the sample of Fig. 1(a), Eq.

(8) results in a surface recombination time  $\tau_s \approx 10 \mu\text{s}$ , which will have a relatively small effect on the  $\approx 400 \text{ ns}$  measured high-injection lifetime.

While considerations in this section have been focused on the high- or low-injection limits and room temperature, in the following section we employ carrier dynamics simulations as well as experimental measurements to investigate how the carrier lifetimes vary over the full range of injection levels and temperatures (100–1000 K).

#### IV. VARIATION OF CARRIER LIFETIME WITH INJECTION AND TEMPERATURE

It is apparent from Fig. 1 that lifetime measurements on the same sample, carried out under different injection conditions, can produce very different results. A similar situation holds with varying temperature. This can be of particular concern, for example, when comparing room temperature measurements to those carried out on an operating device running at elevated temperature. These issues are addressed here by examining the behavior of the carrier lifetime for arbitrary temperature and injection, employing both experimental measurement and carrier dynamics simulations for  $n$ -type 4H-SiC, assuming a single dominant recombination center. The latter follows from the recent identification<sup>30</sup> of the  $Z_1/Z_2$  defect as the center controlling the MCL in this material. When the concentration of this defect is reduced sufficiently, it has been shown recently<sup>32</sup> that other defects or surface recombination can then become dominant.

There are several important parameters that tend to dominate the results of the calculation (as well as the observed behavior). The sensitivity of the calculated lifetimes to varying injection levels is primarily governed by the carrier capture cross sections and the concentrations of both the deep defects and the equilibrium carriers. Although there are several parameters that are temperature dependent, such as capture cross sections and the average thermal velocity of the carriers, the primary contributor to the temperature variation of the lifetime is the depth of the defect level(s) from the band edge, as these enter exponentially in determining the emission rates of the carriers from the deep centers. The specific nature of the deep defect also plays a significant role. In the present case, the  $Z_1/Z_2$  defect has been shown to be a negative- $U$  center<sup>33</sup> with three possible charge states ( $-$ ,  $0$ ,  $+$ ) and two transitions within the gap ( $-/0$  and  $0/+$ ). A calculation of the carrier dynamics must take this internal level structure into account. Recombination at a defect containing two interacting levels is clearly beyond the capability of the simple SRH model. Sah and Shockley<sup>34</sup> have worked out the statistics appropriate to multiply charged defects and Choo<sup>35</sup> has applied this to the transient case in the low-injection limit. By employing numerical simulation for this complex defect, we will examine the full range of injection and temperature variation of the lifetime.

##### A. Carrier dynamics simulation

A schematic of the level structure of  $Z_1/Z_2$  in 4H-SiC is shown in Fig. 3. The defect has been identified as a pair of states close in energy,  $Z_1$  and  $Z_2$ , and thought to represent the

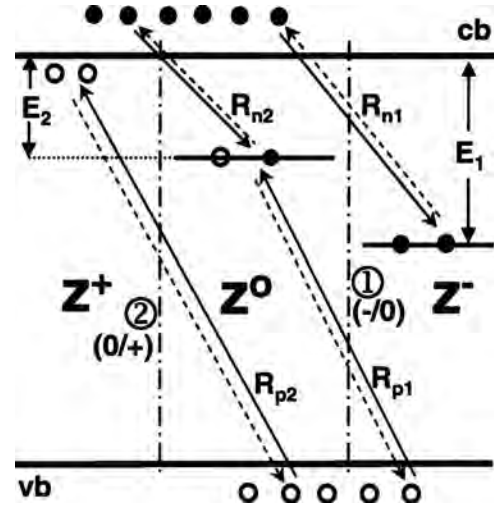


FIG. 3. Schematic level scheme for carrier capture and emission at the  $Z_1/Z_2$  defect. The three charge states of  $Z_1/Z_2$  ( $-$ ,  $0$ ,  $+$ ) are indicated, resulting in two transitions: 1 for ( $-/0$ ) and 2 for ( $0/+$ ). Transitions due to carrier capture or emission are indicated by solid or dashed arrows, respectively, with corresponding trap depths  $E_1$  and  $E_2$ . The net carrier capture rate for each transition is indicated by the  $R_{nj}$  and  $R_{pj}$ .

same defect (identified as a carbon vacancy-related center<sup>36,37</sup>) on cubic and hexagonal lattice sites.<sup>33</sup> For simplicity, however, we will treat this center as a single complex defect. The quoted parameters (binding energies and capture cross sections) that follow, which will be employed in the calculation, represent averages of the values reported in Ref. 33 for the two states. The negative- $U$  nature of the defect means that it can trap two electrons and that the second electron is bound more tightly than the first, due to large lattice relaxation of the  $Z^-$  state. Consequently, in  $n$ -type material the two-electron  $Z^-$  state,  $\approx 0.62 \text{ eV}$  below the conduction band,<sup>33</sup> is the equilibrium charge state at room temperature. Through hole capture or electron emission a ( $-/0$ ) transition to the one-electron  $Z^0$  state [ $\approx E_c - 0.47 \text{ eV}$  (Ref. 33)] can occur, and a second similar transition ( $0/+$ ) leads to the empty  $Z^+$  state. As a result of the large lattice relaxation of the  $Z^-$  state, the energy barrier for thermal emission of an electron also includes a capture barrier,  $\approx 0.07 \text{ eV}$ ,<sup>33</sup> making the total emission barrier for  $Z^- \approx 0.69 \text{ eV}$ .

In Fig. 3, transitions between charge states are represented as diagonal lines, with carrier capture indicated as a solid line and carrier emission as a dashed line. The  $R_{nj}$  and  $R_{pj}$  are net electron and hole capture rates for the transitions  $j=1, 2$  corresponding to ( $-/0$ ) and ( $0/+$ ) transitions, respectively. Referring to the figure, it can be shown that the net carrier capture rates take the form

$$\begin{aligned} R_{n1} &= a_{n1}(nZ^0 - n_1Z^-), \\ R_{n2} &= a_{n2}(nZ^+ - n_2Z^0), \\ R_{p1} &= a_{p1}(pZ^- - p_1Z^0), \\ R_{p2} &= a_{p2}(pZ^0 - p_2Z^+), \end{aligned} \quad (9)$$



where the  $a_{nj}$  and  $a_{pj}$  are electron and hole capture coefficients, e.g.,  $a_{nj} = \sigma_{nj} v_{th,n}$ , with electron and hole capture cross sections  $\sigma_{nj}$  and  $\sigma_{pj}$ , respectively,  $v_{th,n,p} = (3 kT/m_{e,h}^*)^{1/2}$  are the average carrier thermal velocities and  $n$ ,  $p$ , and  $Z^k$  are the electron, hole, and  $Z_1/Z_2$  (in charge state  $k = -, 0, +$ ) concentrations. The quantities  $n_j$  and  $p_j$  are given by<sup>2</sup>  $n_j = N_c \exp[-(E_c - E_j)/kT]$  and  $p_j = N_v \exp[-(E_j - E_v)/kT]$ , with  $N_c(T)$  and  $N_v(T)$  the effective density of states for the conduction and valence bands, respectively, and the  $E_j$  denote the energy separations from the conduction band of the two defect levels  $(-/0)$  and  $(0/+)$ . The time-varying carrier and defect concentrations are determined by the carrier dynamics defined by Eq. (9) and Fig. 3.

It is convenient to carry out the calculations with carrier and defect concentrations defined in terms of equilibrium values and their variations from equilibrium, so that  $n(t) = n_0 + \delta n(t)$ ,  $p(t) = p_0 + \delta p(t)$ , and  $Z^k(t, T) = Z_0^k(T) + \delta Z^k(t, T)$ , where the zero subscripts denote equilibrium values and the initial defect populations are temperature dependent. A calculation of the equilibrium defect concentrations (see Sec. IV C 2) indicates that the  $Z_1/Z_2$  centers are essentially all in the  $Z^-$  state for temperatures  $< 500$  K, due to the depth of the defect levels below the conduction band. In general, however, the equilibrium defect concentrations are temperature dependent. This enters the calculations as a temperature dependent initial condition.

For fixed defect concentration and charge conservation, we also require

$$\sum_k \delta Z^k = 0, \quad (10)$$

$$\delta n - \delta p = \delta Z^0 + 2\delta Z^+.$$

Equation (10) enables the elimination of two of the five time-dependent variables;  $\delta n$ ,  $\delta p$ , and  $\delta Z^k$ . Consequently, along with Eq. (9), the time dependences of the carrier and defect concentrations after the end of the exciting pulse are determined by

$$\begin{aligned} \frac{d\delta n}{dt} &= -(R_{n1} + R_{n2}), \\ \frac{d\delta p}{dt} &= -(R_{p1} + R_{p2}), \\ \frac{d\delta Z^-}{dt} &= R_{n1} - R_{p1}, \end{aligned} \quad (11)$$

where the net capture rates, written in terms of variations from equilibrium, take the form

$$\begin{aligned} R_{n1} &= a_{n1}\{(n_0 + \delta n)[\delta p - \delta n - 2\delta Z^- + Z_0^0] \\ &\quad - n_1[Z_0^+ + \delta Z^-]\}, \\ R_{n2} &= a_{n2}\{(n_0 + \delta n)[\delta n - \delta p + \delta Z^- + Z_0^+] \\ &\quad - n_2[\delta p - \delta n - 2\delta Z^- + Z_0^0]\}, \end{aligned} \quad (12)$$

$$\begin{aligned} R_{p1} &= a_{p1}[(p_0 + \delta p)(Z_0^- + \delta Z^-) \\ &\quad - p_1[\delta p - \delta n - 2\delta Z^- + Z_0^0]], \\ R_{p2} &= a_{p2}[(p_0 + \delta p)[\delta p - \delta n - 2\delta Z^- + Z_0^0] \\ &\quad - p_2(\delta n - \delta p + \delta Z^- + Z_0^+)]. \end{aligned}$$

For  $n$ -type SiC,  $p_0 \ll n_0$ ,  $\delta n$ ,  $\delta p$  and can be neglected. With appropriate initial conditions, the solution to Eqs. (10)–(12) provides the time-dependent carrier and defect concentrations, from which instantaneous carrier lifetimes may then be determined,  $\tau_n(t) = [-(d\delta n/dt)/\delta n]^{-1}$  and  $\tau_p(t) = [-(d\delta p/dt)/\delta p]^{-1}$ .

Similarly, the instantaneous PL decay rate may also be obtained:  $\tau_{PL}(t) = [-(dI_{PL}/dt)/I_{PL}(t)]^{-1}$ . With  $I_{PL}(t)$  in the form of Eq. (5), it is straightforward to show that the PL lifetime is related to the carrier lifetimes through

$$\frac{1}{\tau_{PL}(t)} = \frac{1}{\tau_p(t)} + \frac{1}{\tau_n(t)} \left[ \frac{\delta n(t)}{n_0 + \delta n(t)} \right], \quad (13)$$

where both  $\tau_n(t)$  and  $\tau_p(t)$  depend upon the time-varying defect concentrations. Equation (13) yields the same high- and low-injection PL decay times as noted in Sec. III B,  $\tau_{PL}(\delta n \rightarrow \infty) \rightarrow \tau_{HL}/2$  and  $\tau_{PL}(\delta n \rightarrow 0) \rightarrow \tau_p \rightarrow \tau_{MCL}$ .

The injection level  $g$  enters the calculation as an initial condition for the carrier concentrations:  $\delta n(0) = \delta p(0) \equiv g$ . The temperature variations of the nonequilibrium carrier concentrations and their lifetimes are determined by the temperature dependent parameters in the calculation. The  $n_j$  and  $p_j$  vary as  $T^{3/2} \exp[-E_j/kT]$  and dominate over the temperature dependence of the  $a_{nj}$  and  $a_{pj}$ , which vary as  $T^{1/2}$ , in addition to any temperature variation of the capture cross sections. For  $T > 100$  K, the equilibrium carrier concentration is in the saturation range,<sup>38</sup> so the equilibrium carrier concentration  $n_0$  may be taken as temperature independent.

## B. Calculation parameters

The solution of Eqs. (10)–(12) leads to the determination of the time, injection, and temperature dependence of the carrier concentrations and their lifetimes and of the concentrations of the three  $Z_1/Z_2$  charge states. The extent to which these results are representative of what is observed experimentally is very dependent upon the material parameters employed in the calculation. Many of these have been measured, however, and are available in the literature.

Effective masses for 4H-SiC, necessary for evaluating the valence and conduction band densities of states and the average thermal velocities, have been determined by Son *et al.*<sup>39</sup> Trap depths and electron capture cross sections for  $Z_1/Z_2$  were reported by Hemmingsson *et al.*<sup>33</sup> As noted earlier, the closely spaced  $Z_1$  and  $Z_2$  centers will be treated as a single defect, with averages of their similar parameters employed in the calculation. While Hemmingsson *et al.* have measured the temperature dependent  $(0/-)$  electron capture cross section  $\sigma_{n1}$ , the  $(+ / 0)$  electron capture cross section  $\sigma_{n2}$  reported by this group and by several others<sup>40–43</sup> falls into the range,  $\sigma_{n2} \approx (1-20) \times 10^{-15} \text{ cm}^2$ . This wide range results from the fact that these values are obtained as an



TABLE III. Parameters employed in the numerical solution of Eqs. (10)–(12).

Parameter	Symbol	Value	Reference	Note
−/0 trap depth	$E_1$	0.62 eV	33	a
0/+ trap depth	$E_2$	0.47 eV	33	a
0/− capture barrier	$E_b$	0.07 eV	33	a
0/− $e^-$ capture cross section	$\sigma_{n1}$	$1.5 \times 10^{-15} e^{-0.07/kT}$ cm <sup>2</sup>	33	a
+/0 $e^-$ capture cross section	$\sigma_{n2}$	$(1-20) \times 10^{-15}$ cm <sup>2</sup> $\approx (2-4) \times 10^{-15}$ cm <sup>2</sup>	33 and 40–43 This work	c
−/0 $h^+$ capture cross section	$\sigma_{p1}$	$3.5 \times 10^{-14}$ cm <sup>2</sup>	30	
0/+ $h^+$ capture cross section	$\sigma_{p2}$	$\approx (1-2) \times 10^{-14}$ cm <sup>2</sup>	This work	c
$e^-$ long. effective mass	$m_{e\parallel}^*$	$0.30m_0$	39	
$e^-$ trans. effective mass	$m_{e\perp}^*$	$0.45m_0$	39	
$h^+$ long. effective mass	$m_{h\parallel}^*$	$1.75m_0$	39	
$h^+$ trans. effective mass	$m_{h\perp}^*$	$0.66m_0$	39	
$Z_1/Z_2$ concentration	$N$	$10^{11} - 10^{14}$ cm <sup>−3</sup>		b
Equilibrium carrier concentration	$n_0$	$10^{14} - 10^{15}$ cm <sup>−3</sup>		b

<sup>a</sup>Average of  $Z_1$  and  $Z_2$  values determined in Ref. 33.<sup>b</sup>Typical range of concentrations found in  $n^-$  epilayers.<sup>c</sup>Range of fitted parameter determined for the three samples A, B, and C (Table I).

extrapolation of measured data and whether or not temperature dependence has been assumed for the capture cross section. Because of this uncertainty, the value of  $\sigma_{n2}$  was estimated here by varying  $\sigma_{n2}$  to match the experiment.

The room temperature hole capture cross section for the −/0 transition has been determined experimentally,<sup>30</sup>  $\sigma_{p1} \cong 3.5 \times 10^{-14}$  cm<sup>2</sup>. The cross section for 0/+ hole capture has not been measured, although deep level transient spectroscopy (DLTS) measurements on forward biased  $p-i-n$  structures have shown that  $\sigma_{n2}$  and  $\sigma_{p2}$  should be of roughly comparable magnitudes.<sup>30</sup> Consequently,  $\sigma_{n2}$  was also varied to optimize the agreement between calculated and measured behavior. The remaining parameters are the concentration of  $Z_1/Z_2$  defects  $N$  and the equilibrium carrier concentration  $n_0$ . These vary from one sample to another and typical values are used in the generic calculations. When comparing to experimental data, measured values of  $n_0$  are used. However, as DLTS measurements were not available for the samples studied here, the total defect concentrations were determined directly from the measured low-injection carrier lifetimes,  $\tau_{MCL} = (a_{p1}N)^{-1}$ . The set of parameter values employed in the calculations are summarized in Table III.

## C. Results and discussion

The calculated temporal response of the carrier and defect concentrations will in large part be determined by the complex nature of the defect and by the specific material parameters employed. While this response will vary widely as a function of injection and temperature, there are several qualitative features apparent in Table III that will have a dominating effect on the results. These are (1) the capture cross sections  $\sigma_{n2}(+/0)$ ,  $\sigma_{p1}(-/0)$ , and  $\sigma_{p2}(0/+)$  are all roughly comparable and  $\gg \sigma_{n1}(-/0)$ ; (2) because the band gap of SiC is large and the two charge state transitions are in the upper half of the band gap, the activation energies for hole emission are quite high,  $>2.5$  eV, so that hole emission is essentially negligible for the temperature range considered

here (100–1000 K); and (3) the large depth below the conduction band of the  $Z_1/Z_2$  defect states makes electron emission processes negligible for  $T < 500$  K.

### 1. Dependence on carrier injection

In order to carry out generalized simulations, it was first necessary to obtain reasonable estimates for the parameters  $\sigma_{n2}$  and  $\sigma_{p2}$ . The measured injection dependence of the PL decay time was shown in Fig. 1 for samples A and B. Both dependences were fitted reasonably well by the solution of Eqs. (10)–(12) for  $\sigma_{n2} \cong (2-4) \times 10^{-15}$  cm<sup>2</sup> and  $\sigma_{p2} \cong (1-2) \times 10^{-14}$  cm<sup>2</sup>, as shown by the solid lines in Fig. 1. These same capture cross sections also provided a reasonable fit to the temperature dependence of the PL decay time for sample C (see next section). Using these parameters, simulations exhibiting general trends in the recombination kinetics could then be carried out, such as those shown in Fig. 4.

Figure 4(a) shows the simulated time dependence of the carriers and the  $Z_1/Z_2$  charge states at 300 K at high initial injection ( $g = 1 \times 10^{16}$  cm<sup>−3</sup>) for a typical  $n^-$  epilayer with  $N = 1 \times 10^{13}$  cm<sup>−3</sup> and equilibrium carrier concentration  $n_0 = 4 \times 10^{14}$  cm<sup>−3</sup>. At 300 K the defects are initially all in the  $Z^-$  state. It should be noted that the dependence of the carrier lifetime upon injection can be seen qualitatively from the change in the decay rate of the carriers, as increasing time corresponds to a monotonically decreasing nonequilibrium carrier concentration. The figure shows that the return to equilibrium after a short excitation pulse can be followed through four stages of decay. The first phase (denoted as “I” in the figure) is dominated by rapid hole capture [on a time scale  $(a_{p1}g)^{-1} \cong 240$  ps] by the  $Z^-$  state, rapidly depleting the  $Z^-$  concentration and building up a substantial population of  $Z^0$  and  $Z^+$ .

Phase II defines the “high-injection” regime. At high injection,  $\delta n \cong \delta p \gg n_0$  and the nonequilibrium electron and hole concentrations decay at the same rate:  $\tau_n \cong \tau_p = \tau_{HL}$ . For clarity we first assume  $T \leq 500$  K, so that carrier emission can be neglected ( $n_1, n_2 \ll \delta n$ ), although extension to arbi-

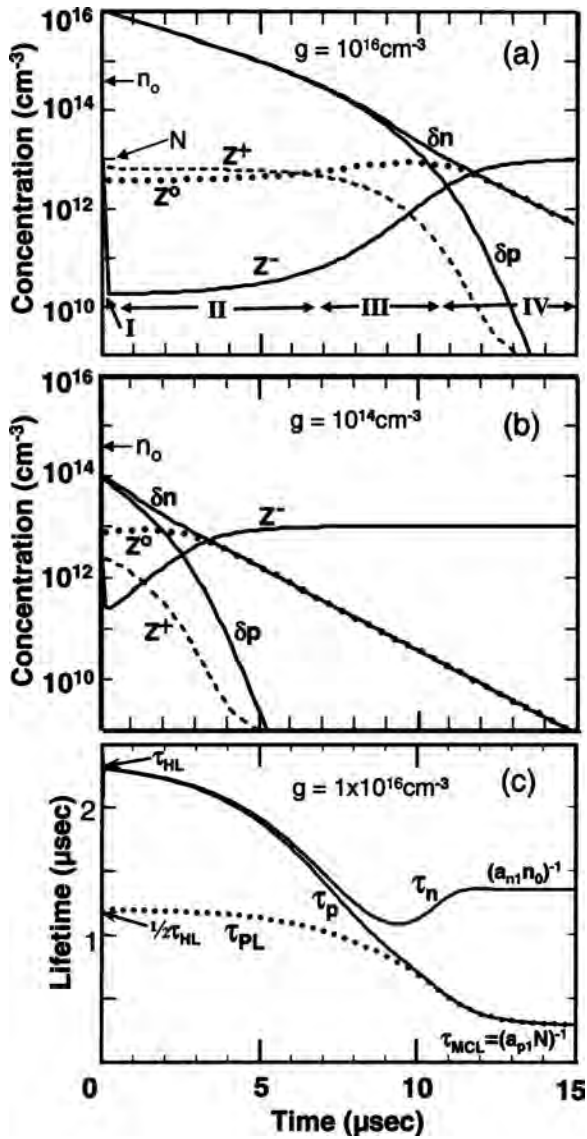


FIG. 4. Simulated time dependence of the carrier concentrations and defect charge states following a short, above-gap optical pulse, for (a)  $1 \times 10^{16} \text{ cm}^{-3}$  injection and (b)  $1 \times 10^{14} \text{ cm}^{-3}$  injection. Typical defect and equilibrium carrier concentrations of  $N = 1 \times 10^{13} \text{ cm}^{-3}$  and  $n_0 = 4 \times 10^{14} \text{ cm}^{-3}$ , respectively, are assumed. In (a) four stages of decay of the carrier system are indicated. The corresponding evolution of the PL and carrier lifetime are shown in (c).

trary temperature is straightforward. The time dependence of the  $Z^-$  and  $Z^+$  concentrations can be determined from  $dZ^-/dt = R_{n1} - R_{p1}$  and  $dZ^+/dt = R_{p2} - R_{n2}$  (see Fig. 3). From Eq. (9), this can be written ( $T \leq 500 \text{ K}$ ), for the high injection regime, as

$$\begin{aligned} \frac{dZ^-(t)}{dt} + a_{p1} \delta n Z^-(t) &= a_{n1} \delta n Z^0(t), \\ \frac{dZ^+(t)}{dt} + a_{n2} \delta n Z^+(t) &= a_{p2} \delta n Z^0(t). \end{aligned} \quad (14)$$

The characteristic times over which  $Z^-$  and  $Z^+$  vary,  $(a_{p1} \delta n)^{-1}$  and  $(a_{n2} \delta n)^{-1}$ , respectively, are rather short at high injection:  $\approx 240 \text{ ps}$  and  $1.5 \text{ ns}$  at  $1 \times 10^{16} \text{ cm}^{-3}$  injection. For times much longer than this, the  $Z^k(t)$  approach their

quasisteady-state (QSS) levels ( $t \rightarrow \infty$ ), with the  $dZ^k/dt \approx 0$ . Equation (14) then becomes

$$\begin{aligned} a_{p1} Z_{\text{QSS}} &\equiv a_{n1} Z_{\text{QSS}}^0, \\ a_{n2} Z_{\text{QSS}}^+ &\equiv a_{p2} Z_{\text{QSS}}^0. \end{aligned} \quad (15)$$

As long as the decaying carrier concentration remains high enough to stay within the high injection regime, the defect concentrations will be slow-varying near their QSS levels—as can be seen in the region “II” in Fig. 4(a). Equation (15) reflects the same balance of electron and hole capture at each transition ( $-/0$  and  $0/+$ ) that occurs during thermal equilibrium. Equation (15) and the condition  $\sum Z^k = N$  allows the determination of the QSS defect concentrations,  $Z_{\text{QSS}}^k$ , in terms of  $N$  and the capture coefficients. These appear in the Appendix, but without restriction on temperature.

As the decaying nonequilibrium carrier concentration approaches  $n_0$ , the electron and hole concentrations begin to diverge and the decay enters into phase III, a transition between high and low injection regimes. The depleted  $Z^-$  concentration is slowly restored through  $0/-$  electron capture while the  $Z^+$  concentration is reduced by  $+/0$  electron capture. The restoration of the  $Z^-$  concentration leads to an increase in the  $-/0$  hole capture rate, resulting in an accelerated decay of  $\delta p$ . Phase III is similar to decay under low-injection excitation, as seen by comparing to Fig. 4(b), which represents decay with a lower initial injection of  $1 \times 10^{14} \text{ cm}^{-3}$ . Aside from a time shift of several microseconds ( $\mu\text{s}$ ), corresponding to the time for the high injection carrier concentration in Fig. 4(a) to decay down to  $\approx 1 \times 10^{14} \text{ cm}^{-3}$ , the two sets of decays are essentially identical. It is also apparent from Fig. 4(b) that under low injection conditions phase II is absent.

In the final, low-injection stage of decay, phase IV, where the  $Z^+$  are essentially depleted,  $Z^- \approx N$  and  $\delta p \ll \delta n \ll n_0$ , the nonequilibrium electron concentration must be identical to  $Z^0$ , where essentially all of the remaining trapped holes reside. With  $Z^- \approx N$ ,  $\delta p$  decays with the MCL  $\tau_p = (a_{p1} N)^{-1}$ , while the  $0/-$  transition of the last recombining electrons leads to the low level electron lifetime  $\tau_n \equiv (a_{n1} n_0)^{-1}$ .

The decay for the high-injection case in Fig. 4(a) may also be described by the time dependence of the instantaneous carrier lifetimes, as shown in Fig. 4(c). Here phase II (high injection,  $\tau_n \approx \tau_p$ ) and phase IV (low-injection limit) are quite apparent. The PL decay time is also shown, with a clear evolution from high injection at early times ( $\tau_{\text{PL}} = \tau_{\text{HL}}/2$ ) to low injection ( $\tau_{\text{PL}} = \tau_{\text{MCL}}$ ) behavior at later times. The complicated behavior of  $\tau_n$  in phase III results from the rapid decrease in the  $Z^+$  concentration, which reduces the total electron capture rate and increases  $\tau_n$ . The small  $0/-$  electron capture coefficient ( $a_{n1}/a_{n2} \ll 1$ ) makes this effect particularly apparent.

An expression for the high-injection lifetime can be obtained from the QSS defect concentrations in Eq. (15) (see Appendix), since at high injection (and  $T \leq 500 \text{ K}$ )  $\tau_{\text{HL}}^{-1} = -(d\delta n/dt)/\delta n \equiv (a_{n1} Z_{\text{QSS}}^0 + a_{n2} Z_{\text{QSS}}^+)$ . This results in the high level lifetime

$$\tau_{\text{HL}}^{-1} = \left(1 + \frac{a_{p2}}{a_{n2}} + \frac{a_{n1}}{a_{p1}}\right)^{-1} (a_{n1} + a_{p2})N. \quad (16)$$

Since for 4H-SiC,  $a_{n1} \ll a_{p1}$ ,  $a_{p2}$  the high injection lifetime for  $T \leq 500$  K simplifies to

$$\tau_{\text{HL}}^{-1} \cong \frac{a_{n2}a_{p2}}{a_{n2} + a_{p2}}N. \quad (17)$$

In the low injection limit, the minority carrier lifetime was given by  $\tau_{\text{MCL}} = (a_{p1}N)^{-1}$ . Combining this with Eq. (17) provides an expression for the ratio of high-injection to low-injection lifetimes

$$(\tau_{\text{HL}}/\tau_{\text{MCL}}) \cong \frac{a_{p1}(a_{n2} + a_{p2})}{a_{n2}a_{p2}}. \quad (18)$$

This ratio is only a function of the capture coefficients for  $T < 500$  K and may be compared directly to experiment. At 300 K, using the parameters in Table III, we find  $(\tau_{\text{HL}}/\tau_{\text{MCL}})_{300 \text{ K}} \cong 10$ . Since the PL decay time at high injection is half the carrier lifetime

$$(\tau_{\text{HL}}/\tau_{\text{MCL}})_{\text{PL}} = \frac{\tau_{\text{PL}}(\delta n \rightarrow \infty)}{\tau_{\text{PL}}(\delta n \rightarrow 0)} = \frac{1}{2}(\tau_{\text{HL}}/\tau_{\text{MCL}}). \quad (19)$$

Consequently, the ratio of high- to low-injection PL lifetimes is expected to be  $(\tau_{\text{HL}}/\tau_{\text{MCL}})_{\text{PL}, 300 \text{ K}} \cong 5$ . This agrees quite well with the measured injection dependences shown for samples A and B in Figs. 1(a) and 1(b).

With the inclusion of thermal emission, similar results are obtained without restriction on temperature, as indicated in the Appendix.

## 2. Dependence on temperature

Since the temperature dependence of the decaying non-equilibrium carrier concentration is expected to be dominated by carrier emission from deep centers, increasing temperature will lead to longer lifetimes, as the emission process tends to repopulate the decaying carrier concentration. Since the emission barrier for holes from  $Z_1/Z_2$  is so large, as was noted earlier, hole emission processes do not contribute significantly for  $T < 1000$  K.

In Fig. 5(a) the temperature dependence of the PL decay time measured for sample C (open squares) is compared to the simulated behavior (closed circles). The injection level of the experiment was set at  $1 \times 10^{14} \text{ cm}^{-3}$ . The calculated PL lifetime exhibits a sharp increase near 500 K, reproducing the observed behavior reasonably well. The simulation was carried out with  $\sigma_{n2} = 3 \times 10^{-15} \text{ cm}^2$  and  $\sigma_{p2} = 1.4 \times 10^{-14} \text{ cm}^2$ —very close to the values used to calculate the injection dependences for samples A and B (see Table I). The experimental data are compared to that of Kordina *et al.*<sup>44</sup> (filled diamonds). Over their common range of temperature the two sets of data agree reasonably well. However, the experiment does not reproduce the sharpness of the “knee” of the calculated curve near 500 K. This may be a result of the model, which assumes that the  $Z_1/Z_2$  defect is the only recombination center contributing to the lifetime. A more gradual transition near 500 K could result from contribution to the lifetime from additional recombination centers that

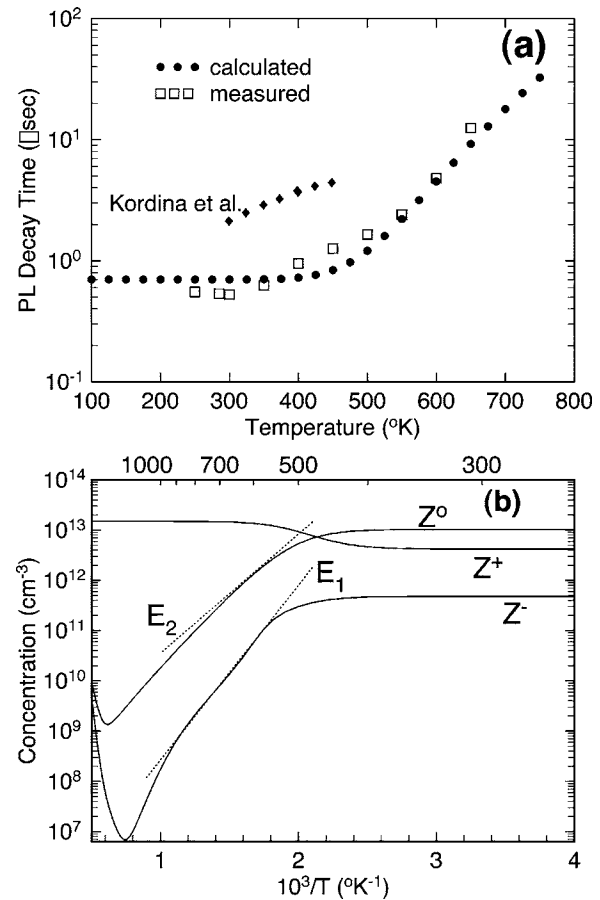


FIG. 5. (a) Measured temperature dependence of the PL lifetime for sample C (open squares) compared to the simulated behavior (solid circles) using the parameters in Tables I and III. The temperature dependence of the lifetime reported by Kordina *et al.* (Ref. 44) shown as filled diamonds, compares well with the present measurements. The temperature dependence of the three  $Z_1/Z_2$  charge state concentrations resulting from the simulation in (a) at  $t \approx 0.5 \mu\text{s}$  is shown in (b), where the effects of electron emission and, at higher temperature, hole emission are evident.

have a lower thermal activation energy than  $Z_1/Z_2$ . One reasonable candidate is the shallow boron acceptor, with  $E_A = 0.27 \text{ eV}$ ,<sup>45,46,49</sup> that is an important hole trap in typical  $n^-$  epilayers. These centers are compensated in  $n$ -type material and could contribute to minority carrier capture. With increasing temperature, the trapped holes can become thermalized, increasing the free carrier concentration, and consequently, the carrier lifetime, in the temperature range below 500 K. The calculated temperature dependence just above 500 K was found to be primarily the result of electron emission from  $Z^0$  ( $0/+$  transitions), with emission barrier  $E_2 = 0.47 \text{ eV}$  (Table I).

The simulated temperature dependences of the three  $Z_1/Z_2$  charge states corresponding to Fig. 5(a) are shown in Fig. 5(b) for  $t = 0.5 \mu\text{s}$  after the exciting pulse. It is apparent from the figure that the knee near 500 K is associated with a decrease in the  $Z^0$  concentration and a corresponding increase in the  $Z^+$  concentration, clearly indicating the  $0/+$  transition. As expected, the decreasing  $Z^-$  and  $Z^0$  concentrations at increasingly higher temperatures also reflect thermal activation energies close to  $E_1$  and  $E_2$ , respectively. However, the actual temperature dependence above 500 K is



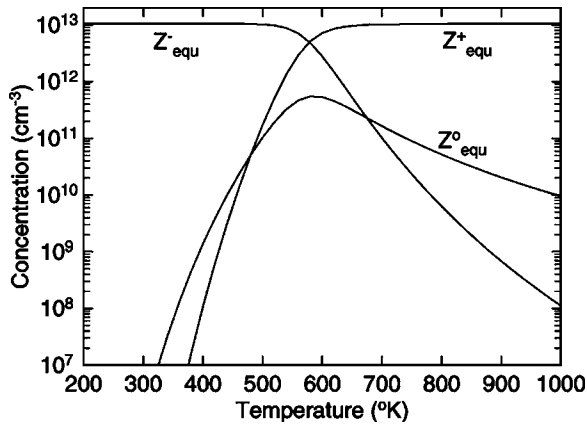


FIG. 6. Calculated temperature dependence of the equilibrium  $Z_1/Z_2$  charge states. The population of the equilibrium charge states determines the initial conditions of the carrier dynamics simulations. The negative- $U$  nature of the defect prevents the  $Z^0$  state from gaining significant population, as noted in the DLTS studies of Hemmingsson *et al.* (Ref. 33).

complex, as  $T^{3/2}$  contributions from the  $n_j$ ,  $T^{1/2}$  contributions from the capture coefficients and the temperature dependent initial conditions combine with the thermally activated behavior. As the temperature approaches 1300 K, thermal hole emission becomes activated, appearing in Fig. 5(b) first as a rapid increase in  $Z^-$  as holes from  $Z^0$  are emitted, and then as a rapid increase in  $Z^0$  near 1600 K as holes are emitted from  $Z^+$ .

While varying the temperature affects the carrier lifetime primarily through the temperature dependent parameters in Eqs. (11) and (12), it also changes the equilibrium distribution of the three  $Z_1/Z_2$  charge states. This changes the conditions existing at the arrival of the exciting pulse and can affect the resulting nonequilibrium carrier decay. This was taken into account as a temperature dependent initial condition in the solution of Eq. (11). These conditions are determined by the temperature dependence of the equilibrium charge state concentrations, which can be evaluated by setting  $d\delta Z^-/dt = R_{n1} - R_{p1} = 0$  and  $d\delta Z^+/dt = R_{p2} - R_{n2} = 0$ , with the  $R_{jk}$  of Eq. (12) determined for the equilibrium condition  $\delta n = \delta p = 0$ . The resulting temperature dependence is shown in Fig. 6. It is apparent from the figure that in equilibrium and below 500 K, essentially all the defects are in the  $Z^-$  state, while above 650 K they are essentially all in the  $Z^+$  state. In the narrow temperature window between these limits, the  $Z^0$  state never populates more than about 5% of the defects. In essence, with increasing temperature, the equilibrium defect concentration switches from “-” to “+” charge states. This is a result of the negative- $U$  nature of  $Z_1/Z_2$ : With all the defects in the  $Z^-$  state at low temperature and the depth of the  $Z^-$  trap greater than that of  $Z^0$ , when the temperature is increased high enough to thermalize carriers from  $Z^-$ , the resulting  $Z^0$  centers (with lower trap depth) are immediately thermalized to the  $Z^+$  state. This is precisely the same mechanism reported by Hemmingsson *et al.*<sup>33</sup> to explain the quenching of the  $Z^0$  DLTS signal and to identify the  $Z_1/Z_2$  DLTS signature as an effective  $-/+$  transition.

### 3. Contribution of the $EH_6/EH_7$ defect to the carrier lifetime

The carrier dynamics simulations thus far have assumed a single deep defect—the  $Z_1/Z_2$  center. However, the DLTS spectra of typical  $n^-$  4H-SiC epilayers are dominated by two electron traps:  $Z_1/Z_2$  and  $EH_6/EH_7$ . It is, therefore, useful to consider the extent to which  $EH_6/EH_7$  affects the carrier lifetimes. Toward this end, simulations were carried out incorporating both  $Z_1/Z_2$  and  $EH_6/EH_7$  defects. The latter is a midgap trap,  $E_{6/7} \cong 1.55$  eV, with electron capture cross sections reported<sup>42,46–50</sup> in the range  $(1–90 \times 10^{-14} \text{ cm}^2)$ .

An additional electron trap with filled and empty charge states  $M^-$  and  $M^0$ , respectively, may be incorporated into the simulations by including additional electron and hole capture rates,  $R_{n3}$  and  $R_{p3}$ , in Eq. (9), analogous to those of  $Z_1/Z_2$ , as well as an additional relationship in Eq. (11):  $d\delta M^-/dt = R_{n3} - R_{p3}$ , where  $M = M^- + M^0$  is the total concentration of  $EH_6/EH_7$  defects. The capture rates are  $R_{n3} = a_{n3}(nM^0 - n_3M^-)$ , and  $R_{p3} = a_{p3}(pM^- - p_3M^0)$ . Here  $a_{n3}$  and  $a_{p3}$  are the electron and hole capture coefficients and  $n_3$  and  $p_3$  are analogous to their definitions for  $Z_1/Z_2$  and are both negligible for the temperature range considered here, due to the large depth of the midgap trap. Additionally, the charge conservation relationship in Eq. (10) must also be modified to reflect the additional defect.

The wide range of reported electron capture cross sections noted earlier results from the fact that these were determined by extrapolations of Arrhenius plots of the emission time constant. However, Hemmingsson *et al.*<sup>50</sup> have determined  $\sigma_{n3}$  directly by measuring the dependence of the capacitance transient on the width of the filling pulse. They determined from this measurement that  $\sigma_{n3} = 5 \times 10^{-15} \text{ cm}^2$ . Consequently, this value will be used in the simulations for  $EH_6/EH_7$ . The hole capture cross section,  $\sigma_{p3}$ , has not been measured for  $EH_6/EH_7$ . However, DLTS measurements as a function of forward bias in  $p-i-n$  diode structures, described briefly in Sec. IV B for the  $Z_1/Z_2$  defect, were carried out for the  $EH_6/EH_7$  defect as well.<sup>30</sup> While the  $Z_1/Z_2$  concentrations decreased significantly with increasing forward bias, indicating a charge state transition due to capture of the injected holes, the  $EH_6/EH_7$  signal was unaffected by the presence of a large injected hole concentration at high bias. This indicated<sup>30</sup> a small capture cross section for holes for  $EH_6/EH_7$ . This, coupled with a substantial capture cross section for electrons, indicates that  $EH_6/EH_7$  would be expected to be an effective electron trap but an ineffective recombination center. To reflect this in the simulations, a hole capture cross section of  $1 \times 10^{-17} \text{ cm}^2$  was assumed.

The calculated evolution of the carrier and  $Z_1/Z_2$  defect concentrations, similar to that of Fig. 4(a), is shown in Fig. 7 at an initial injection of  $1 \times 10^{16} \text{ cm}^{-3}$  for three  $EH_6/EH_7$  concentrations  $(0, 1, 5) \times 10^{14} \text{ cm}^{-3}$ . It is clear from the figure that the  $EH_6/EH_7$  concentration must substantially exceed  $1 \times 10^{14} \text{ cm}^{-3}$  in order to affect the results, as the calculated behavior for the two lower concentrations was identical. While such high levels can be attained through electron irradiation,<sup>46</sup> the concentration of  $EH_6/EH_7$  in typical as-grown epilayers is usually<sup>46,47</sup>  $\leq 1 \times 10^{13} \text{ cm}^{-3}$  and is roughly comparable to that of  $Z_1/Z_2$ , as the two defects are



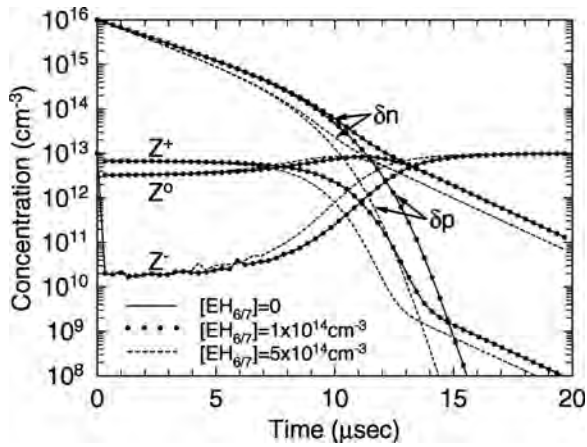


FIG. 7. Simulated time dependence of the  $Z_1/Z_2$  charge states and carrier concentrations, analogous to Fig. 4(a), but with the inclusion of both  $Z_1/Z_2$  and  $EH_6/EH_7$  defects. The solid, dotted, and dashed lines correspond to  $EH_6/EH_7$  concentrations of 0,  $1 \times 10^{14} \text{ cm}^{-3}$ , and  $5 \times 10^{14} \text{ cm}^{-3}$ , respectively. Initial injection is at  $1 \times 10^{16} \text{ cm}^{-3}$ .

thought to both be related to the carbon vacancy.<sup>36,37</sup> The ineffectiveness of  $EH_6/EH_7$  in influencing the lifetime is clearly a result of the small hole capture cross section: With the defects all filled at equilibrium and carrier emission negligible due to the depth of the defect, interaction between  $EH_6/EH_7$  and the carrier system must involve hole capture, which is, therefore, the rate-limiting process.

The effect of introducing  $EH_6/EH_7$  defects is to reduce the carrier lifetimes, while the magnitude of this effect depends on the defect concentration and capture cross sections. This can be seen in more detail using extended versions of Eqs. (9) and (11) that include  $EH_6/EH_7$ . Thus,

$$\tau_n^{-1} = -\frac{d\delta n/dt}{\delta n} = \frac{(R_{n1} + R_{n2} + R_{n3})}{\delta n} = (\tau_n^{-1})_{Z1/Z2} + (\tau_n^{-1})_{EH6/7}, \quad (20)$$

where the additional contribution to the lifetime by  $EH_6/EH_7$  is

$$(\tau_n^{-1})_{EH6/7} = \frac{R_{n3}}{\delta n} = a_{n3}M^0(t) \left(1 + \frac{n_0}{\delta n}\right). \quad (21)$$

Because  $a_{p3}$  is small, it is difficult to buildup a substantial  $M^0$  concentration through hole capture. Consequently, the contribution from  $EH_6/EH_7$  in Eqs. (20) and (21) is expected to be relatively small as well. As is evident in Fig. 7, this can be compensated for to some degree if a large  $EH_6/EH_7$  concentration exists.

A similar case exists for holes and the contribution of  $EH_6/EH_7$  to the hole lifetime is

$$(\tau_p^{-1})_{EH6/7} = \frac{R_{p3}}{\delta p} = a_{p3}M^-(t). \quad (22)$$

At high injection, the contribution of  $EH_6/EH_7$  to the high-level lifetime  $\tau_{HL}$  is determined by its QSS charge state concentrations

$$\tau_{HL}^{-1} = (\tau_{n,QSS})^{-1} = (\tau_{n,QSS})_{Z1/Z2}^{-1} + (\tau_{n,QSS})_{EH6/7}^{-1}, \quad (23)$$

where the contribution of  $EH_6/EH_7$  to the high-level lifetime is

$$(\tau_{HL,QSS})_{EH6/7}^{-1} = a_{n3}M_{QSS}^0 = \frac{a_{n3}a_{p3}}{a_{n3} + a_{p3}}M. \quad (24)$$

It is clear from Eqs. (22) and (24) that the small hole capture cross section also limits the contribution of  $EH_6/EH_7$  to both the hole lifetime and the high-injection level lifetime.

## V. SUMMARY

The preceding discussion has focused on the relationship between disparate carrier lifetime measurements, as the measurements may not be comparable due to differences in the physical lifetimes being measured or to different measurement conditions. As the carrier lifetime is often viewed as a measure of material quality and of suitability for device applications, this relationship becomes a significant consideration. The results of the previous sections provide a framework for assessing the equivalence of independent lifetime measurements and for applying corrections when necessary, so that a direct comparison may be performed. While the simulated variations with injection level or temperature appearing in Sec. IV may be used as a guide, relative corrections may also be obtained through carrier dynamics simulations. The simulations have, for the most part, assumed  $n^-$  4H-SiC dominated by a single lifetime killer, the  $Z_1/Z_2$  defect.<sup>30</sup> As material growth continues to mature and incorporation of this defect is reduced significantly, other defects may take on a dominant role in determining the lifetime. In such cases, the approach in Sec. IV remains applicable, although the nature of the defect and the corresponding details in setting up the simulation will generally be different.

Considerations of the three optical techniques described in Sec. III elucidated the similarities and differences between the high- and low-injection lifetimes determined by these measurements, as summarized in Table II. These differences can lead to discrepancies in reported lifetimes if appropriate corrections are not applied. Ideally, such a comparison should include a broad range of lifetime measurement techniques—both optical and electrical. While this was not practical in the present case, a careful study along these lines would be a valuable contribution. It has been noted<sup>1</sup> that comparison between optical and electrical lifetime measurements may not be straightforward, as defects in device structures have different effects on optical and electrical measurements. On the other hand, it would seem that if the detailed conditions (e.g., injection, temperature, etc.) within the sampled region of a device were known for both types of measurement, appropriate corrections (e.g., Sec. IV) could be applied to enable a fair comparison of the lifetimes. There are, of course, difficulties in this, as the sampled regions are often very different for the two types of measurement and it can be difficult to accurately obtain the necessary parameters that reflect the measurement conditions in a specific region of a device structure.

The simulations were employed to show general trends in the decay of the nonequilibrium carriers. Reasonable agreement with experiment was obtained, leading to values for the 300 K 0/+ capture cross sections  $\sigma_{n2}$  and  $\sigma_{p2}$ , which were necessary to carry out the generalized simulations. From these simulations, and for high initial carrier injection, four phases of decay were identified, including a high-injection phase (not present with low initial injection) in which the populations of the three defect charge states are in a quasisteady-state condition and remain slow varying until the carrier concentrations become comparable to that of the equilibrium carriers. The high-injection lifetime,  $\tau_{HL}$ , is determined from the QSS defect concentrations and is primarily a function of the capture coefficients and the total defect concentration. From this a simple expression for the ratio of the high- to low-injection lifetimes was determined and found consistent with experiment. The results of the simulations were heavily impacted by the negative- $U$  nature of the defect and the resulting internal level structure, as well as the actual values of the material parameters. In particular, the small 0/- electron capture cross section, in part a result of the large lattice relaxation of the  $Z^-$  state, has a significant effect on the carrier dynamics. The simulated temperature dependence was in reasonable agreement with experiment, reflecting weak temperature dependence below 500 K and activated behavior at higher temperature due to electron emission from  $Z^0$ . At higher temperatures electron emission from  $Z^-$  begins to contribute and near 1300 K the simulations predict the onset of efficient hole emission.

The simulations were extended to consider the effect of a second defect,  $EH_6/EH_7$ , on the carrier lifetime. Using a measured value for  $\sigma_{n3}$ , and the qualitative observation that  $\sigma_{p3}$  is small, the simulations suggest that for as-grown material, where the  $EH_6/EH_7$  and  $Z_1/Z_2$  concentrations are not too far apart, there is little contribution to the lifetime from this defect. This is directly a result of the small hole capture cross section, which defines  $EH_6/EH_7$  as an effective electron trap but an ineffective recombination center.

## ACKNOWLEDGMENTS

This work was supported in part by the Office of Naval Research. The author would like to thank A. Y. Polyakov for important contributions during the initial phase of this work and for a thorough reading of the manuscript, J. D. Caldwell for measurement of the microwave photoconductivity map, and A. Shrivastava and T. S. Sudarshan for kindly supplying the 52  $\mu\text{m}$  epitaxial layer.

## APPENDIX: INCLUSION OF THERMAL EMISSION

By including carrier emission, at high injection ( $\delta p \approx \delta n$ ), Eq. (14) can be written without limitations on temperature as

$$\begin{aligned} \frac{dZ^+}{dt} + [a_{n2}\delta n + a_{p2}p_2(T)]Z^+ &= [a_{p2}\delta n + a_{n2}n_2(T)]Z^0, \\ \frac{dZ^-}{dt} + [a_{p2}\delta n + a_{n1}n_1(T)]Z^- &= [a_{n1}\delta n + a_{p1}p_1(T)]Z^0. \end{aligned} \quad (\text{A1})$$

As with Eq. (14), at high injection the  $Z^k(t)$  vary rapidly before reaching their QSS levels. With  $dZ^k/dt \approx 0$  in QSS and using  $\Sigma Z^k = N$  and Eq. (A1), the  $Z_{\text{QSS}}^k$  are determined for  $T < 1000$  K ( $p_1 = p_2 \approx 0$ ) as

$$\begin{aligned} Z_{\text{QSS}}^- &= \left( \frac{N}{D} \right) \left[ \frac{a_{p1}}{a_{n1}} + \frac{n_1(T)}{\delta n} \right]^{-1}, \\ Z_{\text{QSS}}^0 &= \frac{N}{D}, \end{aligned} \quad (\text{A2})$$

$$\begin{aligned} Z_{\text{QSS}}^+ &= \left( \frac{N}{D} \right) \left[ \frac{a_{p2}}{a_{n2}} + \frac{n_2(T)}{\delta n} \right], \\ D &= 1 + \frac{a_{p2}}{a_{n2}} + \frac{n_2(T)}{\delta n} + \left[ \frac{a_{p1}}{a_{n1}} + \frac{n_1(T)}{\delta n} \right]^{-1}. \end{aligned}$$

At very high temperature, of course, the hole emission in Eq. (A1) would have to be included. Using Eqs. (9) and (11) under high injection conditions ( $\delta n \gg n_0$ ), the high-level lifetime becomes

$$\begin{aligned} \tau_n^{-1} &= \tau_{\text{HL}}^{-1} = \left[ -\frac{d\delta n/dt}{\delta n} \right]_{\text{HL}} \\ &= a_{n1} \left( Z_{\text{QSS}}^0 - \frac{n_1 Z_{\text{QSS}}}{\delta n} \right) + a_{n2} \left( Z_{\text{QSS}}^+ - \frac{n_2 Z_{\text{QSS}}}{\delta n} \right). \end{aligned}$$

Inserting the QSS defect concentrations from Eq. (A2), this becomes

$$\tau_{\text{HL}}^{-1} = \left\{ a_{p2} + a_{n1} \left[ 1 - \frac{n_1}{\delta n} \left( \frac{a_{p1}}{a_{n1}} + \frac{n_1}{\delta n} \right)^{-1} \right] \right\} \left( \frac{N}{D} \right), \quad (\text{A3})$$

which reduces to Eq. (16) for  $n_j/\delta n \rightarrow 0$ . With Eq. (A3) and  $\tau_{\text{MCL}} = (a_{p1}N)^{-1}$ , the ratio  $\tau_{\text{HL}}/\tau_{\text{MCL}}$  can be constructed for temperatures below 1000 K.

<sup>1</sup>M. E. Levinshtein, T. T. Mnatsakanov, P. Ivanov, J. W. Palmour, S. L. Rumyantsev, R. Singh, and S. N. Yurkov, IEEE Trans. Electron Devices **48**, 1703 (2001).

<sup>2</sup>W. Shockley and W. T. Read, Phys. Rev. **87**, 835 (1952).

<sup>3</sup>S. G. Sridhara, T. J. Eperjesi, R. P. Devaty, and W. J. Choyke, Mater. Sci. Eng., B **61–62**, 229 (1999).

<sup>4</sup>A. Galeckas, P. Grivickas, V. Grivickas, V. Bikbajevs, and J. Linnros, Phys. Status Solidi A **191**, 613 (2002).

<sup>5</sup>W. M. Bullis and H. R. Huff, J. Electrochem. Soc. **143**, 1399 (1996).

<sup>6</sup>M. L. Polignano, F. Cazzaniga, A. Sabadini, G. Queirolo, A. Cacciato, and A. DiBartolo, Mater. Sci. Eng., B **42**, 157 (1996).

<sup>7</sup>T. L. Chu and E. D. Stokes, J. Appl. Phys. **49**, 2996 (1978).

<sup>8</sup>S. A. Reshanov and G. Pensl, Mater. Sci. Forum **483–485**, 417 (2005).

<sup>9</sup>D. K. Schroder, *Semiconductor Material and Device Characterization* (Wiley, Hoboken, 2006), p. 389.

<sup>10</sup>R. N. Hall, Phys. Rev. **87**, 387 (1952).

<sup>11</sup>V. Grivickas, A. Galeckas, and J. Linnros, Lith. J. Phys. **37**, 473 (1997).

<sup>12</sup>K. Neimontas, R. Aleksiejunas, M. Sudzius, K. Jarasiunas, and P. Bergman, Mater. Sci. Forum **483–485**, 413 (2005).

<sup>13</sup>D. J. Sandiford, Phys. Rev. **105**, 524 (1957).

<sup>14</sup>G. K. Wertheim, Phys. Rev. **109**, 1086 (1958).

- <sup>15</sup>K.C. Nomura and J.S. Blakemore, Phys. Rev. **112**, 1607 (1958).
- <sup>16</sup>K.C. Nomura and J.S. Blakemore, Phys. Rev. **121**, 734 (1961).
- <sup>17</sup>B. G. Streetman, J. Appl. Phys. **37**, 3137 (1966).
- <sup>18</sup>J. Linnros, J. Appl. Phys. **84**, 275 (1998).
- <sup>19</sup>J. Waldmeyer, J. Appl. Phys. **63**, 1977 (1988).
- <sup>20</sup>D. K. Schroder, R. N. Thomas, and J. C. Swartz, IEEE Trans. Electron Devices **ED-25**, 2543 (1978).
- <sup>21</sup>A. Galeckas, J. Linnros, M. Frischholz, and V. Grivickas, Appl. Phys. Lett. **79**, 365 (2001).
- <sup>22</sup>A. Galeckas, J. Linnros, V. Grivickas, U. Lindefelt, and C. Hallin, Appl. Phys. Lett. **71**, 3269 (1997).
- <sup>23</sup>A. Galeckas, V. Grivickas, J. Linnros, H. Bleichner, and C. Hallin, J. Appl. Phys. **81**, 3522 (1997).
- <sup>24</sup>E. Biedermann, Solid State Commun. **3**, 343 (1965).
- <sup>25</sup>V. Grivickas, A. Galeckas, P. Grivickas, and J. Linnros, Mater. Sci. Forum **338-342**, 555 (2000).
- <sup>26</sup>M. Kunst and G. Beck, J. Appl. Phys. **60**, 3558 (1986).
- <sup>27</sup>R. K. Ahrenkiel, in *Semiconductors and Semimetals*, edited by R. K. Ahrenkiel and M. S. Lundstrom (Academic, New York, 1993), Vol. 39, pp. 39-150.
- <sup>28</sup>M. Boulou and D. Bois, J. Appl. Phys. **48**, 4713 (1977).
- <sup>29</sup>A. B. Sproul, J. Appl. Phys. **76**, 2851 (1994).
- <sup>30</sup>P. B. Klein, B. V. Shanabrook, S. W. Huh, A. Y. Polyakov, M. Skowronski, J. J. Sumakeris, and M. J. O'Loughlin, Appl. Phys. Lett. **88**, 052110 (2006).
- <sup>31</sup>P. Grivickas, J. Linnros, and V. Grivickas, J. Mater. Res. **16**, 524 (2001).
- <sup>32</sup>K. Danno, D. Nakamura, and T. Kimoto, Appl. Phys. Lett. **90**, 202109 (2007).
- <sup>33</sup>C. G. Hemmingsson, N. T. Son, A. Ellison, J. Hang, and E. Janzén, Phys. Rev. B **58**, R10119 (1998).
- <sup>34</sup>C. T. Sah and W. Shockely, Phys. Rev. **109**, 1103 (1958).
- <sup>35</sup>S. C. Choo, Phys. Rev. B **1**, 687 (1970).
- <sup>36</sup>K. Danno and T. Kimoto, J. Appl. Phys. **100**, 113728 (2006).
- <sup>37</sup>L. Storasta and H. Tsuchida, Appl. Phys. Lett. **90**, 062116 (2007).
- <sup>38</sup>S. M. Sze, *Physics of Semiconductors*, 2nd ed. (Wiley, New York, 1981), p. 25.
- <sup>39</sup>N. T. Son, P. N. Hai, W. M. Chen, C. Hallin, B. Monemar, and E. Janzén, Phys. Rev. B **61**, R10544 (2000).
- <sup>40</sup>T. Tawara, H. Tsuchida, S. Izumi, I. Kamata, and K. Izumi, Mater. Sci. Forum **457-460**, 565 (2004).
- <sup>41</sup>T. Dalibor, G. Pensl, H. Matsunami, T. Kimoto, W. J. Choyke, A. Schöner, and N. Nordell, Phys. Status Solidi A **162**, 199 (1997).
- <sup>42</sup>H. Fujiwara, K. Danno, T. Kimoto, T. Tojo, and H. Matsunami, J. Cryst. Growth **281**, 370 (2005).
- <sup>43</sup>I. Pintilie, L. Pintilie, K. Irscher, and B. Thomas, Appl. Phys. Lett. **81**, 4841 (2002).
- <sup>44</sup>O. Kordina, J. P. Bergman, C. Hallin, and E. Janzén, Appl. Phys. Lett. **69**, 679 (1996).
- <sup>45</sup>D. Menichelli, M. Scaringella, F. Moscatelli, M. Bruzzi, and R. Nipoti, Diamond Relat. Mater. **16**, 6 (2007).
- <sup>46</sup>L. Storasta, J. P. Bergman, C. Hallin, and E. Janzén, Mater. Sci. Forum **389-393**, 549 (2002).
- <sup>47</sup>K. Danno, T. Kimoto, and H. Matsunami, Appl. Phys. Lett. **86**, 122104 (2005).
- <sup>48</sup>G. Alfieri, E. V. Monakhov, B. G. Svensson, and M. K. Linnarsson, J. Appl. Phys. **98**, 043518 (2005).
- <sup>49</sup>J. Zhang, L. Storasta, J. P. Bergman, N. T. Son, and E. Janzén, J. Appl. Phys. **93**, 4708 (2003).
- <sup>50</sup>C. G. Hemmingsson, N. T. Son, O. Kordina, E. Janzén, J. L. Lindström, S. Savage, and N. Nordell, Mater. Sci. Eng., B **46**, 336 (1997).